1 **Lanthanide tetrads in normalized rare element patterns of of zircon from the**

2 **Koktokay No. 3 granitic pegmatite, Altay, NW China**

3

4 TANG YONG[1], ZHANG HUI[1*]

5

6 [1]Key Laboratory of High-temperature and High-pressure Study of the Earth's Interior,

7 Institute of Geochemistry, Chinese Academy of Sciences, 46 Guanshui Road, Guiyang,

8 Guizhou, 550002, P.R. China

9 The first author: TANG YONG

10 E-mail: tangyong@vip.gyig.ac.cn

11 *Corresponding author: ZHANG HUI

12 E-mail:87165753@qq.com

13 **ABSTRACT**

14 Individual crystals of zircon, from the Koktokay No.3 granitic pegmatite vein, are

15 variably altered and consist of three types of domains distinguished on the basis of

16 textures and compositions. The pristine domains possess normal chondrite-normalized

17 rare earth element (REE) patterns. Domains affected by metamictizaion are enriched in U

18 and Th. The presence of abundant fractures, dense pores and, the enrichments of

19 non-formula elements imply that these metamict domains have been altered by a later

20 hydrothermal fluid. Tetrads observed in these altered domains are likely to have been

21 generated by this alteration event.

22 **Keywords**: Zircon; REE tetrads; alteration; pegmatite; Altay

INTRODUCTION

23

24   Chondrite-normalized rare earth element (REE) patterns, which have three

25   discontinuity points at Gd, between Nd and (Pm), and between Ho and Er, can be divided

26   into four segments (La-Nd; Pm-Gd; Gd-Ho; Er-Lu). When these segments are convex

27   unpward or concave downward, this is defined as "M-type or W-type lanthanide tetrads"

28   (Masuda et al. 1987). In past decades, many investigators focused on the lanthanide

29   tetrads in highly evolved granitic system because the tetrads can be used as a

30   geochemical indicator to constrain the evolution of igneous and hydrothermal systems.

31   All these previous results indicate that granitic whole rocks and separated minerals from

32   highly evolved granitic systems may exhibit M-type tetrads(Bau 1996, 1997; Jahn et al.

33   2001; Liu and Zhang 2005; Masuda and Akagi 1989; Monecke et al. 2002, 2007; Wu et al.

34   2011 and references in) or W-type tetrads rarely (Monecke et al. 2011). However, the

35   geochemical processes that are responsible for the tetradst are not yet fully understood.

36   Several genetic models have been proposed to interpret the origin of the tetrads in

37   geological materials: (i) fractional crystallization of REE-rich accessory minerals during

38   the crystallization of silicate melt (Foster 1998; Jolliff et al. 1989; McLennan 1994; Pan

39   and Breaks 1997; Yurimoto et al. 1990; Zhao and Cooper 1993); (ii) fluid-melt

40   interaction during crystallization of the silicate melt (Irber 1999); (iii) surface

41   weathering(Takahashi et al. 2002); (iv) F-rich magmatic fluid-melt interaction (Veksler et

42   al. 2005); (v) fluid immiscibility and preferential partitioning of REE between vapor and

43   coexisting liquid (Monecke et al. 2011).

44   Many of the previous studies have focused on whole rocks. Compared with whole

45   rocks, the advantage of individual mineral phase is its ability to preserve geological

46   events such as formation, metamorphism and alteration through the change of texture and

47   composition. Zircon commonly occurs in magmatic, metamorphic and sedimentary rocks.

48   It is a host for significant fractions of the whole-rock abundance of some trace elements

49   such as REE (Hoskin and Schaltegger 2003). The normalized rare earth element pattern

50   of unaltered igneous zircons is characterized by a steeply-rising slope from the LREE to

51   the HREE with a positive Ce-anomaly and negative Eu-anomaly. Unusually, some

52   zircons from the Koktokay No.3 granitic pegmatite exhibit a significant M-type tetrads.

53   The aim of the present work is to investigate the possible mechanism that result in the

54   tetrads in zircons from the pegmatite via the analysis of the texture, major and trace

55   element.

56   **GEOLOGICAL BACKROUND**

57   Koktokay No.3 pegmatite is located near the town of Koktokay and is a well-known,

58   highly fractionated and zoned granitic pegmatite which hosts the largest Li-Be-Nb-Ta-Cs

59   pegmatite-type deposit in China. This pegmatite is hosted by metagabbro which

60   embraced by gneissic biotite granite (Fig.1). Between the pegmatite and the metagabbro,

61   there is a thin contact zone with a thickness of several cm. The metagabbro and andbiotite

62   granite were dated at ca. 408 Ma and 409 Ma by SHRIMP zircon U-Pb analyses,

63   respectively (Wang et al. 2006). Koktokay No.3 pegmatite was dated using different

64   isotopic dating methods and the data ranged from 210 to 220 Ma (Che et al. 2015; Liu et

65   al. 2014; Wang et al. 2007).

66   Spatially, the No.3 pegmatite has two parts: an oval-shaped cupola in the upper part

67   and a vein that dips gently at the bottom. The overall shape of this pegmatite looks like a

68   solid hat. The cupola strikes NNW and dips NE at an angle of 40~80°; it is about 250 m

69   long, 150 m wide, and reaches to depths of 250 m. The cupola outcrop is pear shaped.

70   The gently dipping vein strikes NW and dips SW at an angle 10~40°, has a thickness of

71   20~60m, and a terrace-shaped appearance;its exact boundary have yet to be determined

72   (Zou and Li 2006)

73   The No.3 pegmatite has a perfectly concentric textural zonation. Based on the

74   mineral assemblages, and textural characteristics, nine distinct zones are distinguished in

75   cupola from the outermost zone inwards (Fig.2):

76   (1) Graphic zone (zone I): mainly composed of microcline and quartz with minor

77   muscovite and surrounded by quartz-muscovite shell.

78   (2) Saccharoidal albite zone (zone II): consists of dominant whit fine-grained albite

79   (60 vol.%), microcline (22 vol.%) and quartz (16 vol.%). Accessory minerals include

80   beryl, apatite, zircon, and spesartite.

81   (3) Blocky microcline zone (zone III): huge, blocky microcline with an outer contact

82   of saccharoidal albite and inner contact of muscovite-quartz.

83   (4) Muscovite-quartz zone (zone IV): composed of 60 vol% muscovite-quartz and

84   30 vol% blocky microcline.

85   (5) Cleavelandite-spodumene zone (zone V): rich in spodumene, containing 65 vol%

86   cleavelandite-spodumene and 30 vol% quartz-spodumene.

87   (6) Quartz-spodumene zone (zone VI): contains lithium mineralization, 65 vol%

88   quartz-spodumene and 35 vol% cleavelandite-spodumene.

89   (7) Platy albite-muscovite zone (zone VII): mainly consisted of platy

90   albite-muscovite with small amount of quartz-spodumene and blocky quartz.

91   (8) Lepidolite-platy albite zone (zone VIII) : lens-shaped, mainly composed of

92   lepidolite-platy albite with small amounts of muscovite-platy albite.

93   (9) Blocky quartz (zone IX): comprised of 79 vol% blocky quartz and 21 vol%

94   blocky microcline.

95   Previous studies of fluid inclusion, mineralogy, and rare earth element geochemistry

96   have suggested that the crystallization evolution of the Koktokay No.3 pegmatite could

97   be at least divided into two stages: one magmatic stage and the other

98   hydrothermal-related one. The magmatic stage includes zones I to IV (the outer zones)

99   (Zhu et al. 2000; Liu and Zhang 2005; Zhang et al. 2004, 2008a, 2008b). The types of

100   inclusions in the outer zones include melt-inclusions and crystal-rich fluid-inclusions

101   (Zhu et al. 2000). Zircons from zone II is intergrowth with albite that is the main

102   rock-forming mineral in this zone. Therefore, zircon from this zone undoubtedly is part of

103   a primary, magmatic assemblage.

104

105

106

107   **MATERIALS AND METHODS**

108   Samples for zircon analyses were collected from the zone II in cupola part. About 10

109   kg of raw rocks from zone II were crushed and sieved to 60~80 mesh. Zircon grains were

110   separated by standard methods (including gravity concentration and magnetic separation).

111   10 zircon grains were finally handpicked under a binocular microscope. These selected

112   grains were mounted in epoxy, and then were polished until the cores of grains were

113   exposed.

114   Cathodoluminescence (CL) imaging was done at the State Key Laboratory of

115   Continental Dynamics, Northwest University, China, using a FEI Quanta 400 scanning

116   electron microscope equipped with an Oxford IE 350 energy dispersive spectroscopy

117   system and a Gatan MonoCL3+ detector. The operating conditions included an

118   accelerating voltage of 15 kV and a bean current beam of 20 nA.

119   Major elements analyses of zircon grains and backscattered electron images were

120   carried out with a JXA-8100 electron probe micro-analyzer (EPMA) equipped with four

121   wavelength-dispersive spectrometers at the State Key Laboratory of Geological Processes

122   and Mineral Resources, School of Earth Sciences, China University of Geosciences. The

123   EMPA was operated at an accelerating voltage of 15 KV and a beam current of 20 nA.

124   The beam diameter was ca. 1 μm. The following standards were used for quantitative

125   elemental analyses: zircon (Zr, Si), Hf metal (Hf), UO_2 (U), ThO_2 (Th), apatite (P),

126   pyrope (Al), almandine (Fe), diopside (Ca). Peaks and backgrounds for most elements

127   were measured with counting times of 20 and 10 s, respectively, apart from Si (10 s on

128   peak; 5 s on background). All data were reduced using the ZAF correction program.

129   Trace elements analyses of zircons were performed using the laser-ablation,

130   inductively coupled plasma mass spectrometer (LA-ICPMS) at the Key Laboratory of

131   Continental Dynamics, Northwest University, China. A detailed compilation of the

132   instrument and data acquisition parameters are presented in Yuan et al. (2004). The

133   GeoLas 200 M laser-ablation system equipped with a 193 nm ArF-excimer laser and a

134   homogenizing imaging optical system was used in connection with an Agilent 7500

135   ICP-MS. Helium was used as the carrier gas to enhance the transport efficiency of ablated

136   materials. Laser spot size and frequency were 30 μm and 8 Hz, respectively. The

137   LA-ICP-MS measurements were carried out using peak jumping mode and dwell time for

138   each isotope was set 6 ms.Raw data were processed using the ICPMSData Cal (Liu et al.

139   2008). REE concentrations were calibrated by using ^{29}Si as internal standard and

140   NIST610 as an external reference material.

RESULTS

142   Zircon grains are brown, opaque, stubby prismatic to dipyramidal shapes, and in the

143   range of 200 to 500μm in size. These zircon grains appear to be closely intergrown with

144   albite (Fig. 3a). These crystals have a low CL response, and at first glance, they are

145   typical of externally euhedral but internally patchy textured zircons (Fig. 3b). More

146   complex zoning textures are revealed by BSE imaging. There are abundant fractures in

147   all analyzed 10zircon grains (Fig. 3c), and three different domains within a single zircon

148   grain (Fig. 3d), herein designated as A, B, and C, are identified on the basis of mean

7

149   atomic number and texture. As shown in Fig.3d, domain A is usually located at the rim

150   and characterized by its smooth surface and uniform bright grey contrast; Domain B is

151   volumetrically most significant and, characterized by a low density of micro-pores and is

152   darker in the BSE image than domain A. Some uranium oxide inclusions are present in

153   this domain (UO_2= 93.76 wt%, ThO_2=2.62 wt%); Domain C is distinguished by dense

154   pores and a mosaic texture, and is the darkest part in the image.

155   Representative results of EPMA obtained from different spots within each of the

156   three domains are shown in Table 1. Domain A has a normal oxide totals (~100 wt.%). As

157   shown in Fig.4, it is characterized by very low concentrations of U, Th, and non-formula

158   elements (like Ca and Al), and has Si and Zr contents typical of normal crystalline

159   Hf-rich zircon (containing 4.85~8.24 wt.% HfO_2). The other two domains have much

160   lower oxide totals (84.01 to 96.31 wt.%). Domain B is characterized by relatively high

161   levels of U and Th, moderated enrichments of non-formula elements such as Al and Ca,

162   and low Si, and Zr (Fig. 4); domain C is also enriched in U and Th, meanwhile it has the

163   highest concentrations of non-formula elements, and usually contains several wt% of

164   Al_2O_3, and CaO (Fig. 4).

165   The concentrations of REE in zircons are listed in Table 2, and the

166   chondrite-normalized REE patterns are plotted in Fig. 5. Domain A has the lowest total

167   REE content, ranging from 16.59 to 25.30 ppm, and domain C shows the highest REE

168   contents (198.4~390.90 ppm). All REE patterns are characterized by pronounce negative

169   Eu anomalies and positive Ce anomalies. Besides the Eu and Ce anomalies, the REE

8

170   patterns show two curves with a discontinuity point between Ho and Er, which resemble

171   M-type tetrads. The tetrads were quantified according to Monecke et al. (2002). As

172   shown in Fig. 5, domain A shows an absence of tetrads or very weak M-type tetrads.

173   However, the low concentration of REE in domain A may lead to large analytical errors,

174   so it cannot be fully excluded that the weak tetrad effect in these areas may represent an

175   analytical artifact. In contrast, domains B and C show a significant M-type tetrads,

176   especially in the third segment (from Gd to Ho).

177

178   **DISCUSSION**

179   **Genesis of Zircons**

180   Extreme variations in compositions and structures of zircons from zone II are

181   revealed by EMPA and BSE imaging. Three domains can be easily identified within a

182   single zircon grain (Fig. 3d). Domain B is characterized by relatively high levels of U and

183   Th. The radioactive decay of U and Th causes structural damage, which can strongly

184   affect bulk physical properties of zircon crystals (Ewing et al. 2003). Radiation damage

185   (metamictization) not only decreases the stability of zircon against aqueous solution , but

186   also create abundant fractures that enable fluid to penetrate the internal structure of zircon.

187   Geisler et al. (2001, 2003) confirmed via experimental methods that metamict zircon can

188   effectively be altered by various aqueous solutions. Incorporations of non-formula

189   elements such as Al and Ca into zircons are usually ascribed to alteration (Geisler et al.

190   2007). High levels of Al_2O_3 and CaO in domain B imply that these domains have

9

191 undergone fluid alteration. For the same reason, domain C should be the most-alteration

192 portion, because it contains the highest concentrations of Al_2O_3 and CaO.

193   Domain A is characterized by very low concentrations of U, Th, and non-formula

194 elements, has Si and Zr contents typical of normal crystalline Hf-rich zircon, and mainly

195 located at the rim. The formation of these growth rims can be ascribed to the presence of

196 an aqueous fluid or a melt. In terms of U-Pb isotopic compositions and textures, the

197 generation of domain A should be linked with the melt, due to the following evidences: 1)

198 As mentioned above, the pristine zircons from zone II were directly crystallized from

199 melt; 2) Domain A has almost same U-Pb ages to domain B that undergoes least

200 alteration (Table 2); 3) Domain A is usually broken by fractures that are created by

201 metamictization, so it is suggest that domain A should be formed prior to the beginning of

202 metamictization.

203   Judging from compositions and textures, the following processes can account for the

204 generation of zircon from zone II. Firstly, U and Th-rich zircons crystallized from a melt,

205 and then early U and Th-rich zircon was replaced by U and Th-poor zircon as a result of

206 progressive changes in melt composition during the fractional crystallization process.

207 Secondly, differential metamictization causes volume expansion of the U-rich domains

208 with consequent fracturing of the more resistant and brittle low-U domains. The

209 metamictization not only decreases the stability of zircon against aqueous solution , but

210 also create abundant fractures that enable fluid to penetrate the internal structure of zircon.

211 Finally, thesemetamictareas were altered by a later hydrothermal fluid.

10

The generation of tetrads

212

213   Unaltered magmatic zircons from different crustal source-rocks have very similar

214 chondrite-normalized REE pattern, which characterized by a steeply-rising slope from La

215 to Lu with a positive Ce anomaly and negative Eu-anomaly (Hoskin and Schaltegger

216 2003). In contrast, hydrothermal andhydrothermally-altered zircons vary greatly in REE

217 abundances and pattern due to differences in hydrothermal mineral assemblages, fluid

218 origins, fO_2, as well as other factors (Hoskin and Schaltegger 2003; Pettke et al. 2005).

219 As shown in Fig.3, LREE concentrations generally increase with increasing alteration,

220 while HREE is not obviously variable. Even though the tetrads in LREE (from La to Eu)

221 are difficult to recognize due to the existence of Ce anomalies and non-occurrence of Pm

222 in natural samples, the REE patterns of Domain B and C show a significant M-type

223 tetrads in the HREE (from Gd to Lu).

224   REE tetrads are often observed in REE patterns of mineral and rock samples from

225 highly evolved peraluminous granite systems. Liquid immiscibility between fluoride melt

226 and silicate melt (e.g., Veksler et al. 2005), fractional crystallization of accessory

227 minerals (e.g., Yurimoto et al. 1990), and fluid-melt interaction (e.g., Irber, 1999) have

228 been proposed to account for the granitic melt tetrad effect.

229 *Immiscible fluoride and silicate melts*

230   Based on an experimentalexperimental study, Veksler et al. (2005) proposed that

231 liquid immiscibility between fluoride melt and silicate melt is a probable mechanism for

232 REE tetrad effect in Li-F granites. It is known that the development of liquid

11

233   immiscibility might result from fluorine in granitic system, at least 3.5 ~5.9 wt% F in the

234   system should be required (Wang and Huang 2000). It is not easy for the initial granitic

235   magma originated by partial melting of sedimentary rocks to have such a high content of

236   fluorine. In fact, fluorine in whole rock of typical Li-F granites in southern China mainly

237   ranges from 1.0 wt% to 2.3 wt%, and extremely high fluorine only occurs in the last

238   evolution stage of the magmatic systems. As an example, fluorine in dike No. 431

239   topazite at Xianghualing district, southern China can reach up to 7.8 wt% (Zhu et al.

240   1993). Even for the Erzgebirge granites, Germany, its fluorine in whole rocks ranges

241   from 0.3 wt% to 1.0 wt%, and in the later pegmatitic melt from 1.1 wt% to 5.0 wt%

242   (3.5±0.6 wt% F in average, determined by melt inclusions after Webster et al. 1997).

243   Thus, the mechanism for REE tetrad effect in Li-F granites proposed by Veksler et al.

244   (2005) is not suitable to explain the origin of REE tetrad effect in peraluminous magmatic

245   rocks, such as Koktokay No.3 pegmatite, which is characterized by low in fluorine in its

246   initial magma (0.3 ~ 0.4 wt% F after Zhang2001).

247   *Fractional crystallization of individual mineral phases*

248   Fractional crystallization of REE-rich accessory minerals used to be discussed to

249   generate tetrad effect, e.g., garnet (Pan 1997); apatite (Jolliff et al. 1989; McLennan,

250   1994), or monazite (Pan and Breaks 1997; Yurimoto et al. 1990). However, Irber (1999)

251   models the fractional crystallization of such minerals, and finds that the calculated REE

252   patterns show discontinuities at some rare elements, such as Nd, but these patterns lack

253   the basic characteristics of the tetrad effect. Moreover, the fractional crystallization of

12

254   such accessory minerals cannot simultaneously account for the existence of the tetrad

255   effect both in minerals and their host rocks.

256   *Fluid-melt interaction*

257   Irber (1999) proposed that the development of a M-type tetrad effect in whole rock

258   REE patterns is cause by fluid-melt interaction during crystallization of the silicate melt

259   in an open system, whereby a complementary REE pattern with W-type tetrad effect is

260   removed from the solidifying magma by coexisting (or exsolved) fluids. However,

261   Monecke et al. (2002, 2007) suggested that M-type tetrads in samples from magmatic

262   environment could not be explained by removal of a complementary REE pattern by

263   coexisting hydrothermal fluid, as they found that fluorite samples collected from a

264   hydrothermal vein within the endo-contact of the Li-F granite in Germany, show the

265   M-type tetrad effect instead of the W-type tetrad effect. Specifically for Koktokay No.3

266   pegmatite, the mass balance calculation by Liu and Zhang (2005)indicated that

267   interaction of the exsolved hydrothermal fluid with the solidified rocks at early stage

268   could not produce significantly tetrads.

269   *Fluid-vapor separation and subsolidus interaction*

270   The presence of fractures, pores, UO_x inclusions, and the enrichments of

271   non-formula elements imply that these metamict domains are altered by a later

272   hydrothermal fluid. These altered domains exhibit a significant M-type tetrad effect,

273   whereas the REE patterns got by Geisler et al. (2003) from metamict zircon with

274   low-temperature fluid alteration show the smooth HREE patterns, indicating that no

13

275   differential disturbance occurred among the HREE.

276   The SHRIMP zircon U-Pb age is 220±9 Ma for pegmatite zone I (Wang et al.

277   2007).The coltan samples yield a weighted mean $^{206}Pb/^{238}U$ age of 218.0 ±2.0 Ma (Che et

278   al. 2015). In the present work, theweighted mean$^{206}Pb/^{238}U$ ages of zircon from zone II is

279   215.4 Ma. Therefore, the initial time of formation of No.3 pegmatite should be ca. 220

280   Ma. Molybdenite (as a hydrothermal sulfide mineral) coexists with coarse-grained

281   tourmaline, garnet, and hydro-hornblenede in the contact zone between No.3 pegmatite

282   and the wall rock. The Re-Osisochron age forMolybdeniteis 208.8 ± 2.4 Ma (Liu et al.

283   2014), and these ages reflect the lower limit of the fluid phase exsolution. The Ar-Ar ages

284   of micas from No.3 pegmatite concentrate within the range of 170.0~180.0 Ma that

285   corresponds to the latest stage of hydrothermal alteration.

286   The degree of metamictization is a function of U and Th concentration and time of

287   radiation exposure, and can be assessed by simple calculation of the accumulated

288   α-dosage (Murakami et al. 1991).The problem of determining the absolute duration of

289   magmatic-hydrothermal events in magmatic systems has been addressed through time

290   needed to crystallize minerals and cooling model of intrusions. The traditional view

291   suggests that the giant crystals in pegmatites should take many, many years to grow. The

292   combination of U-Pb, Ar-Ar, Re-Os is a tool widely used by ore geologists to bracket the

293   duration of magmatic-hydrothermal events in magmatic systems (Chiaradia et al. 2013).

294   The time available for metamictizaiton is <40 Ma if we accept 220 Ma as the initial time

295   formation of No.3 pegmatite and the 170~180 Ma for micas as the latest stage of

14

296   hydrothermal activity. U and Th concentrations such as in the domain B (ca. 2.5 wt% and

297   0.5 wt%, respectively), accumulate an α-dosage more than 3×10^{15} α-decay events/mg

298   within 40 Ma, and this value reaches to the amount necessary to initiate noticeable

299   changes in a typical zircon structure (e.g. Chakoumakos et al. 1987; Murakami et al.

300   1991). However, the period of 40 Ma is too long according to cooling models. The

301   cooling models reveal that typical dikes of pegmatite can cool quickly below their solidus

302   temperature, and possible to glassy, in just a few days, months, or years (cf. London

303   2008). One of possible explanation for the contradiction between the mineral age and the

304   cooling model is that hydrothermal activity continues a long time after this pegmatite

305   cooling below its solidus temperature. It is more likely that before alteration, zircons

306   radiation exposure has a minimum duration of 7 Ma, ranging from zircons crystallized at

307   215.4 Ma (zircon U-Pb age) to the fluid exsolved at 208.8 Ma (Molybdenite Re-Os age).

308   Considering these zircon grains should contain higher concentrations of U and Th than

309   now, the time of <7 Ma can also accumulate an enough α-dosage to cause the transition

310   from crystalline to metamict state (the highest U and Th contents= ca. 3 wt.% and 2 wt.%,

311   respectively and α-dosage= $\sim 1 \times 10^{15}$ α-decay events/mg). In a word, radiation damage

312   plays an important role in enhancing the reactivity of zircon.

313   Based on the field observation, the main alterations types of wall rock to No.3

314   pegmatite include chloritization and carbonatization. The values of δD and $\delta^{13}C_{PDB}$ for

315   primary fluid inclusions in quartz from pegmatite are -86.6‰~-48.6‰ and -6.4‰, and

316   these values indicate the H_2O and CO_2 are derived from the pegmatitic melt (Zou and Li

15

317   2006). Pure CO_2 inclusions and/or CO_2+H_2O inclusions coexisting with two- and

318   three-phase inclusions are observed in quartz, spodumene and beryl (Zhu et al. 2000).

319   The observed fluid inclusion characteristics are clear evidence for the occurrence of

320   phase separation (cf. Ramboz et al. 1982). The separation of the originally homogeneous

321   hydrothermal fluid is probably in response to the sudden pressure drop. The pressure drop

322   may result from the break of the previous consolidation outer zone and the wall rock.

323   This is consistent with the phenomena that the inner zones can cut through the outer

324   zones and protrude into the wall rock in some local area.

325   The finding that tetrads have only been reported from fluorine-rich

326   magmatic-hydrothermal systems suggests that REE complexation with fluorine is

327   essential (Irber 1999). Except from core zone IX, minor topaz was reported in the other

328   zones; it is more commonly distributed in muscovite-quartz zone and lepidolite-platy

329   albite zone (Zou and Li 2006). This indicates a relatively high F concentration in the

330   pegmatitic melt.

331   The exsolved fluid split into a high-salinity fluid and a coexisting CO_2-rich

332   low-salinity vapor. This process results in the REE fractionation, because of the

333   preferential partitioning of REE-Cl in the fluid phase, whereas REE-F complexes

334   portioned in the CO_2-bearing vapor phase (e.g. Monecke et al. 2011). The CO_2-bearing

335   vapor phase would quickly escapes; meanwhile the fractionated fluid can keep in a long

336   time and interact with the previous crystallized minerals.

337   In a word, the fluid-vapor separation and then the alteration by the fractionated fluid

16

338   contribute to the M-type tetrads in metamict zircon domains in the present work.

IMPLICATIONS

340   Three domains of zircon were distinguished on the basis of textures and

341   compositions within individual crystals of zircon from the Koktokay No.3 granitic

342   pegmatite vein. Domain A is pristine and possesses normal chondrite-normalized REE

343   patterns. Domain B, and especially domain C that characterized by the most enrichment

344   of non-formula elements and REE, are enriched in U and Th, and both are affected by

345   metamictization. The presence of abundant fractures, dense pores and, and the

346   enrichments of non-formula elements imply that these metamict domains, domain B and

347   C, are altered by a later hydrothermal fluid. The M-type tetrad effect observed in these

348   altered domains is a result of the interaction between zircons and the fluid that possesses

349   tetrads.

350

ACKNOWLEDGEMENT

357

358

REFERENCES CITED

360 Bau, M. (1996) Controls on the fractionation of isovalent trace elements in magmatic and
361 aqueous systems: evidence from Y/Ho, Zr/Hf, and lanthanide tetrad effect.
362 Contributions to Mineralogy and Petrology, 123(3), 323-333.

363 Bau, M. (1997) The lanthanide tetrad effect in highly evolved felsic igneous rocks - a
364 reply to the comment by Y. Pan. Contributions to Mineralogy and Petrology, 128(4),
365 409-412.

366 Chakoumakos, B.C., Murakami, T., Lumpkin, G.R., and Ewing, R.C. (1987)
367 Alpha-Decay-Induced Fracturing in Zircon: The Transition from the Crystalline to the
368 Metamict State. Science, 236, 1556-1559.

369 Che, X.-D., Wu, F.-Y., Wang, R.-C., Gerdes, A., Ji, W.-Q., Zhao, Z.-H., Yang, J.-H., and
370 Zhu, Z.-Y. (2015) In situ U–Pb isotopic dating of columbite–tantalite by LA–ICP–MS.
371 Ore Geology Reviews, 65, 979-989.

372 Chiaradia, M., Schaltegger, U., Spikings, R., Wotzlaw, J.-F., and Ovtcharova, M. (2013)
373 How accurately can we date the duration of magmatic-hydrothermal events in
374 porphyry systems?-an invited paper. Economic Geology, 108(4), 565-584.

375 Ewing, R.C., Meldrum, A., Wang, L., Weber, W.J., and Corrales, L.R. (2003) Radiation
376 Effects in Zircon. Reviews in Mineralogy and Geochemistry, 53(1), 387-425.

377 Foster, H.J. (1998) The chemical composition of REE-Y-Th-U-rich accessory minerals in
378 peraluminous granites of the Erzgebirge-Fichtelgebirge region, Germany; Part 2,
379 Xenotime. American Mineralogist, 83, 1302-1315.

380   Geisler, T., Pidgeon, R.T., Kurtz, R., van Bronswijk, W., and Schleicher, H. (2003)

381   Experimental hydrothermal alteration of partially metamict zircon. American

382   Mineralogist, 88(10), 1496-1513.

383   Geisler, T., Schaltegger, U., and Tomaschek, F. (2007) Re-equilibration of Zircon in

384   Aqueous Fluids and Melts. Elments, 3(1), 43-50.

385   Geisler, T., Ulonska, M., Schleicher, H., Pidgeon, R., and van Bronswijk, W. (2001)

386   Leaching and differential recrystallization of metamict zircon under experimental

387   hydrothermal conditions. Contributions to Mineralogy and Petrology, 141(1), 53-65.

388   Hoskin, P.W.O., and Schaltegger, U. (2003) The Composition of Zircon and Igneous and

389   Metamorphic Petrogenesis. Reviews in Mineralogy and Geochemistry, 53(1), 27-62.

390   Irber, W. (1999) The lanthanide tetrad effect and its correlation with K/Rb, Eu/Eu*, Sr/Eu,

391   Y/Ho, and Zr/Hf of evolving peraluminous granite suites. Geochimica et

392   Cosmochimica Acta, 63(3-4), 489-508.

393   Jahn, B.-m., Wu, F., Capdevila, R., Martineau, F., Zhao, Z., and Wang, Y. (2001) Highly

394   evolved juvenile granites with tetrad REE patterns: the Woduhe and Baerzhe granites

395   from the Great Xing'an Mountains in NE China. Lithos, 59(4), 171-198.

396   Jolliff, B.L., Papike, J.J., Shearer, C.K., and Shimizu, N. (1989) Inter- and intra-crystal

397   REE variations in apatite from the Bob Ingersoll pegmatite, Black Hills, South

398   Dakota. Geochimica et Cosmochimica Acta, 53(2), 429-441.

399   Liu, C.-Q., and Zhang, H. (2005) The lanthanide tetrad effect in apatite from the Altay No.

400   3 pegmatite, Xingjiang, China: an intrinsic feature of the pegmatite magma. Chemical

401   Geology, 214(1-2), 61-77.

402 Liu, F., Zhang, Z.-X., Li, Q., Zhang, C., and Li, C. (2014) New precise timing constraint

403   for the Keketuohai No. 3 pegmatite in Xinjiang, China, and identification of its

404   parental pluton. Ore Geology Reviews, 56(0), 209-219.

405 Liu, Y., Hu, Z., Gao, S., Günther, D., Xu, J., Gao, C., and Chen, H. (2008) In situ analysis

406   of major and trace elements of anhydrous minerals by LA-ICP-MS without applying

407   an internal standard. Chemical Geology, 257(1), 34-43.

408 London, D. (2008) Pegmatites. Mineralogical Association of Canada, Special publication

409   10, Quebec.

410 Masuda, A., and Akagi, T. (1989) Lanthanide tetrad effect observed in leucogranite from

411   China. Geochemical Journal, 23, 245-253.

412 Masuda, A., Kawakami, O., Dohmoto, Y., and Takenaka, T. (1987) Lanthanide tetrad

413   effects in nature: two mutually opposite type, W and M. Geochemical Journal,

414   21(119-124).

415 McDonough, W.F., and Sun, S.S. (1995) The composition of the Earth. Chemical

416   Geology, 120(3-4), 223-253.

417 McLennan, S.M. (1994) Rare earth element geochemistry and the "tetrad" effect.

418   Geochimica et Cosmochimica Acta, 58(9), 2025-2033.

419 Monecke, T., Dulski, P., and Kempe, U. (2007) Origin of convex tetrads in rare earth

420   element patterns of hydrothermally altered siliceous igneous rocks from the Zinnwald

421   Sn-W deposit, Germany. Geochimica et Cosmochimica Acta, 71(2), 335-353.

422   Monecke, T., Kempe, U., Monecke, J., Sala, M., and Wolf, D. (2002) Tetrad effect in rare

423   earth element distribution patterns: a method of quantification with application to

424   rock and mineral samples from granite-related rare metal deposits. Geochimica et

425   Cosmochimica Acta, 66(7), 1185-1196.

426   Monecke, T., Kempe, U., Trinkler, M., Thomas, R., Dulski, P., and Wagner, T. (2011)

427   Unusual rare earth element fractionation in a tin-bearing magmatic-hydrothermal

428   system. Geology, 39(4), 295-298.

429   Murakami, T., Chakoumakos, B.C., Ewing, R.C., Lumpkin, G.R., and Weber, W.J. (1991)

430   Alpha-decay event damage in zircon. American Mineralogis, 76, 1510-1532.

431   Pan, Y., and Breaks, F.W. (1997) Rare-earth elements in fluorapatite, Separation Lake

432   area, Ontario; evidence for S-type granite-rare-element pegmatite linkage. The

433   Canadian Mineralogist, 35(3), 659-671.

434   Pettke,   T.,   Audétat,   A.,   Schaltegger,   U.,   and   Heinrich,   C.A.   (2005)

435   Magmatic-to-hydrothermal crystallization in the W-Sn mineralized Mole Granite

436   (NSW, Australia): Part II: Evolving zircon and thorite trace element chemistry.

437   Chemical Geology, 220(3-4), 191-213.

438   Ramboz, C., Pichavant, M., and Weisbrod, A. (1982) Fluid immiscibility in natural

439   processes: Use and misuse of fluid inclusion data: II. Interpretation of fluid inclusion

440   data in terms of immiscibility. Chemical Geology, 37(1-2), 29-48.

441   Takahashi, Y., Yoshida, H., Sato, N., Hama, K., Yusa, Y., and Shimizu, H. (2002) W- and

442   M-type tetrad effects in REE patterns for water-rock systems in the Tono uranium

443   deposit, central Japan. Chemical Geology, 184(3-4), 311-335.

444   Veksler, I.V., Dorfman, A.M., Kamenetsky, M., Dulski, P., and Dingwell, D.B. (2005)

445   Partitioning of lanthanides and Y between immiscible silicate and fluoride melts,

446   fluorite and cryolite and the origin of the lanthanide tetrad effect in igneous rocks.

447   Geochimica et Cosmochimica Acta, 69(11), 2847-2860.

448   Wang, L.K., and Huang, Z.L. (2000) Magmatic segregation and experiments of Li-F

449   granite., p. 217-221. Science Press, Beijing.

450   Wang, T., Hong, D.W., Jahn, B.M., Tong, Y., Wang, Y.B., Han, B.F., and Wang, X.X.

451   (2006) Timing, petrogenesis, and setting of Paleozoic synorogenic intrusions from the

452   Altai Mountains, Northwest China: implications for the tectonic evolution of an

453   accretionary orogen. The Journal of Geology, 114(6), 735-751.

454   Wang, T., Tong, Y., Jahn, B.M, Zou, T.R., Wang, Y.B., Hong, D.W., and Han, B.F. (2007)

455   SHRIMP U-Pb Zircon geochronology of the Altai No. 3 Pegmatite, NW China, and

456   its implications for the origin and tectonic setting of the pegmatite. Ore Geology

457   Reviews, 32(1-2), 325-336.

458   Webster, J.D., Thomas, R., Rhede, D., Forster, H.-J., and Seltmann, R. (1997) Melt

459   inclusions in quartz from an evolved peraluminous pegmatite: Geochemical evidence

460   for strong tin enrichment in fluorine-rich and phosphorus-rich residual liquids.

461   Geochimica et Cosmochimica Acta, 61(13), 2589-2604.

462   Wu, C.Z., Liu, S.H., Gu, L.X., Zhang, Z.Z., and Lei, R.X. (2011) Formation mechanism

463   of the lanthanide tetrad effect for a topaz- and amazonite-bearing leucogranite pluton

464   in eastern Xinjiang, NW China. Journal of Asian Earth Sciences, 42(5), 903-916.

465   Yuan, H., Gao, S., Liu, X., Li, H., Günther, D., and Wu, F. (2004) Accurate U-Pb Age and

466   Trace Element Determinations of Zircon by Laser Ablation-Inductively Coupled

467   Plasma - Mass Spectrometry. Geostandards and Geoanalytical Research, 28(3),

468   353-370.

469   Yurimoto, H., Duke, E.F., Papike, J.J., and Shearer, C.K. (1990) Are discontinuous

470   chondrite-normalized REE patterns in pegmatitic granite systems the results of

471   monazite fractionation? Geochimica et Cosmochimica Acta, 54(7), 2141-2145.

472   Zhang, A.C., Wang, R.C., Hu, H., Zhang, H., Zhu, J.C., and Chen, X.M. (2004) Chemical

473   evolution of Nb-Ta oxides and zircon from the Koktokay No. 3 granitic pegmatite,

474   Altai, northwestern China. Mineral Magazine, 68(5), 739-756.

475   Zhang, A.C., Wang, R.C., Jiang, S.Y., Hu, H., and Zhang, H. (2008a) Chemical and

476   textural features of tourmaline from the spodumene-subtype Koktokay No. 3

477   pegmatite, Altai, northwestern China: A record of magmatic to hydrothermal

478   evolution. The Canadian Mineralogist, 46, 41-58.

479   Zhang, A.C., Wang, R.C., Li, Y.L., Hu, H., Lu, X.C., Ji, J.F., and Zhang, H. (2008b)

480   Tourmalines from the Koktokay No.3 pegmatite, Altai, NW China: spectroscopic

481   characterization and relationships with the pegmatite evolution. European Journal of

482   Mineralogy, 20(1), 143-154.

483   Zhang, H. (2001) The geochemical behavious and mechanisms of incompatible trace

484   elements in the magmatic-hydrothermal transition system: A case study of Altay No.3

485   pegmatite, Xinjiang. I, Ph. D., p. 155-156. nstitute of Geochemistry, Chinese

486   Academy of Sciences (in Chinese with English abstract).

487   Zhao, J.X., and Cooper, J.A. (1993) Fractionation of monazite in the development of

488   V-shaped REE patterns in leucogranite systems: Evidence from a muscovite

489   leucogranite body in central Australia. Lithos, 30(1), 23-32.

490   Zhu, J.C., liu, W.X., and Zhou, F.Y. (1993) Ongonite and topazite in dike No.431 of

491   Xianghuangling district and their spatial zonation and genetic relationship. Acta

492   Petrology Sinica, 9(2), 158-166 (in Chinese with English abstract).

493   Zhu, Y.F., Zeng, Y., and Gu, L. (2006) Geochemistry of the rare metal-bearing pegmatite

494   No. 3 vein and related granites in the Keketuohai region, Altay Mountains, northwest

495   China. Journal of Asian Earth Sciences, 27(1), 61-77.

496   Zou, T.R., and Li, Q.C. (2006) The rare metal and the REE deposits in xinjiang, China.

497   34-51 p. Geological Publishing House, Beijing (in Chinese with English abstract).

498
499
500
501
502
503
504
505
506
507
508
509
510
511
512

513
514   Figure captions:
515

516   FIGURE1 Geological map of Koktotayregion showing the occurrence of No.3 pegmatite

517   FIGURE 2 Internal textural zonation of the Koktokay No.3 pegmatite

518   FIGURE 3 Representative CL and BSE images of zircons: (a) zircon crystals intergrown

519   with albite crystals; (b) Zircon is externally euhedral but internally patchy texture; (c) and

520   (d) abundant fractures, complex textures and alteration, occurrence of UO_x inclusion.

521   FIGURE 4 Diagrams showing the chemical compositions of three domains within zircons

522   FIGURE 5Chondrite-normalized REE patterns of three domains within zircons.

523   Chondrite values are taken from McDonough and Sun (1995).
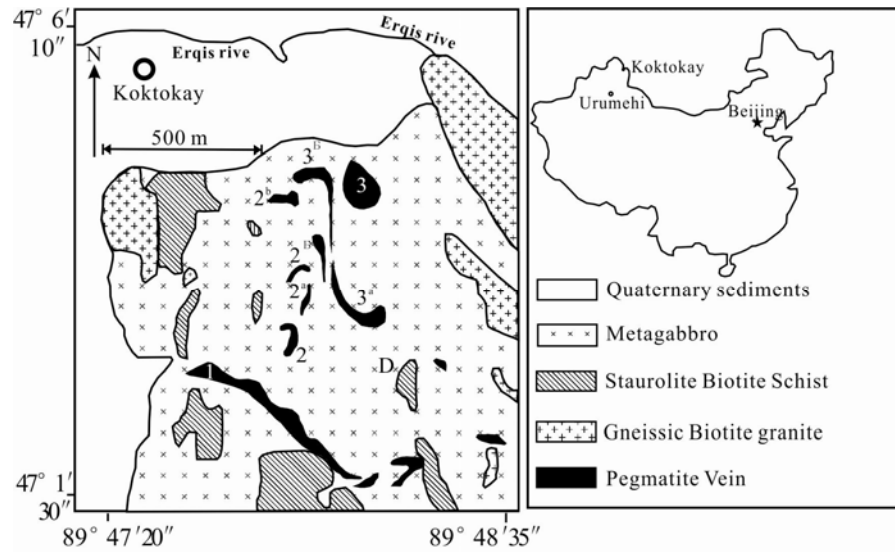
524

525

526

527

528

529

530

531

532

533
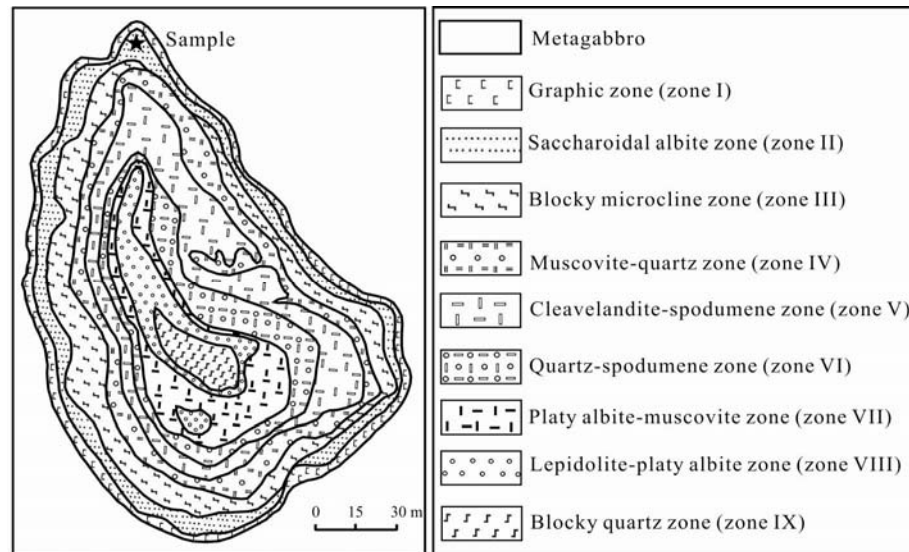
534

535
536
537
538
539
540
541

FIGURE 1

542
543
544
545
546
547
548
549
550
551
552
553
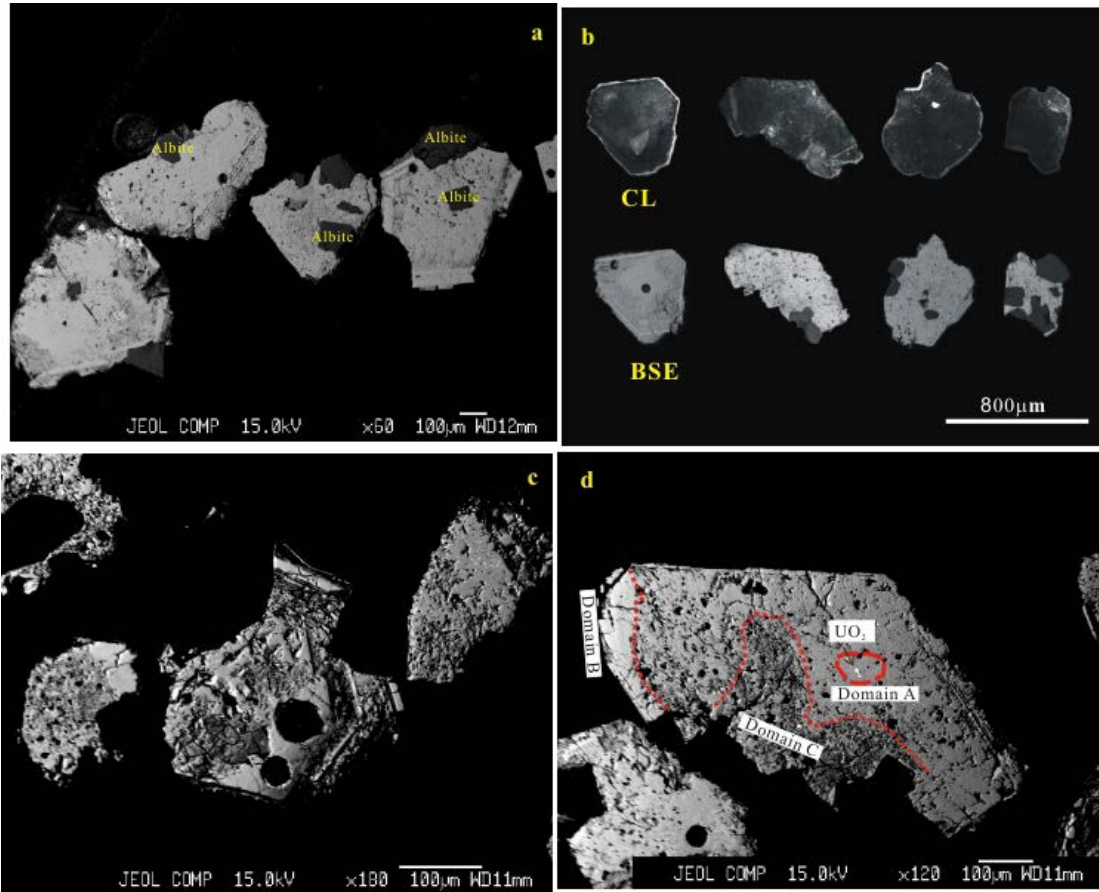554
555
556
557
558

559

560

561

FIGURE 2

562

563

564

565

566

567

568

569

570

571

572

573

574

575

576

577

578

579

580

581

582

583

584

585

586

587

FIGURE 3

588

589
590
591
592
593
594
595
596

28

597

598   FIGURE 4
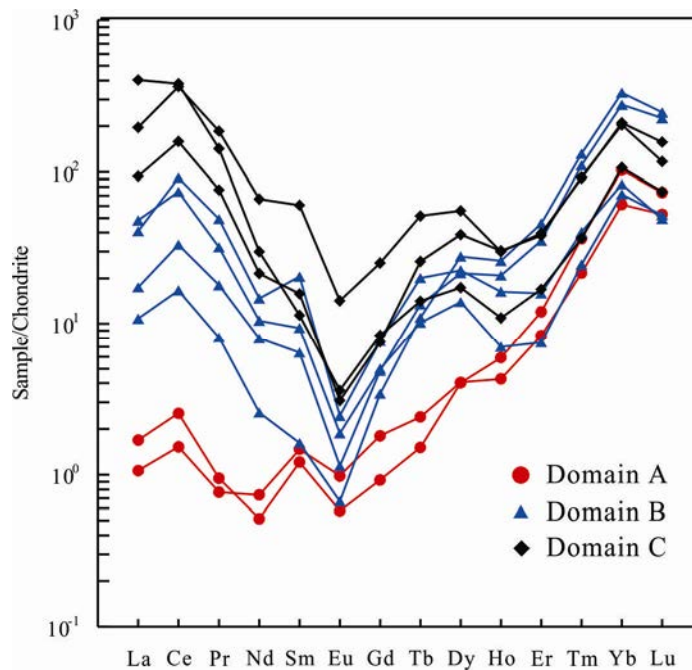
599

600

29
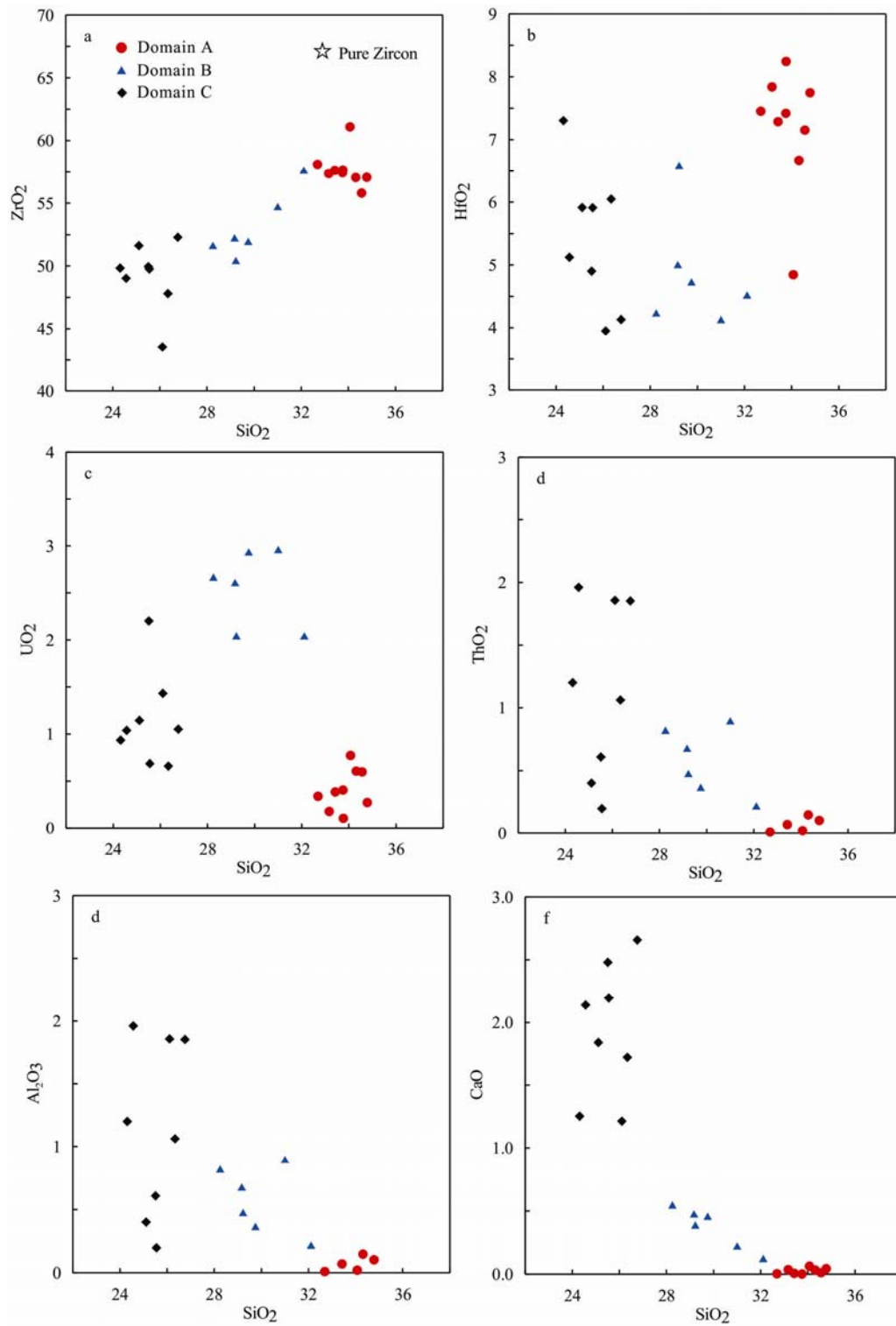
601

602

603

604

605

606

607

608

FIGURE 5

610

611

612

613

614

615

616

617

30

618

619   Table Captions

620   Table 1 Representative EMPA compositions of different domains within zircons from

621   Zone II

622   Table 2 The REE concentrations of different domains within zircons from Zone II

623

624

625
626
627
628
629

31

Table 1 Representative EMPA compositions of different domains within zircons from Zone II

	Domain A					Domain B						Domain C						
	A1	A2	A3	A4	A5	B1	B2	B3	B4	B5	B6	C1	C2	C3	C4	C5	C6	C7
SiO_2	33.75	32.69	33.42	33.76	34.31	32.11	31.00	29.23	29.17	29.75	28.25	25.55	25.11	26.11	26.76	24.31	26.34	25.51
Al_2O_3	0.02	0.01	0.04	0.01	0.11	0.19	0.24	0.47	0.50	0.50	0.53	1.07	1.22	0.90	1.63	1.60	1.57	1.47
FeO	0.06	0.02	0.04	-	-	0.27	0.79	0.79	0.88	0.69	1.09	0.44	0.58	2.96	0.67	0.67	0.52	0.49
CaO	0.00	0.00	0.01	-	0.03	0.12	0.21	0.38	0.47	0.45	0.54	2.20	1.84	1.21	2.66	1.25	1.72	2.48
Na_2O	0.01	0.01	0.00	0.00	0.04	0.11	0.23	0.38	0.37	0.29	0.42	0.05	0.08	0.09	0.05	0.07	0.17	0.03
ZrO_2	57.44	58.10	57.62	57.65	57.05	57.55	54.64	50.34	52.14	51.86	51.55	49.76	51.62	43.52	52.29	49.83	47.80	49.95
HfO_2	7.42	7.45	7.29	8.24	6.67	4.50	4.11	6.57	4.99	4.71	4.22	5.91	5.91	3.95	4.13	7.30	6.05	4.90
UO_2	0.41	0.34	0.39	0.11	0.61	1.03	2.95	2.03	2.60	1.92	2.66	0.69	1.14	1.43	1.05	0.94	0.66	2.20
ThO_2	-	0.01	0.07	-	0.15	0.21	0.89	0.47	0.67	0.36	0.81	0.20	0.40	1.86	1.85	1.20	1.06	0.61
P_2O_5	0.02	-	-	-	-	0.22	0.59	0.72	0.84	0.68	0.88	2.44	2.56	1.98	1.99	2.83	2.71	2.66
total	99.13	98.64	98.86	99.77	98.97	96.31	95.65	91.39	92.63	91.21	90.93	88.30	90.46	84.01	93.07	90.01	88.60	90.30

Dash (-) denotes below the detection limite.

32

633   Table 2 the REE concentrations of different domains within zircons from Zone II

	Domain A		Domain B				Domain C		
	1	2	1	2	3	4	1	2	3
La	0.40	0.25	4.09	2.54	11.27	9.58	22.07	94.41	46.1
Ce	1.53	0.92	20.10	10.04	44.68	55.20	95.87	229.86	220.0
Pr	0.08	0.07	1.60	0.72	2.85	4.37	6.79	12.70	16.5
Nd	0.23	0.33	3.60	1.16	4.75	6.66	9.74	13.55	30.1
Sm	0.18	0.22	0.94	0.24	1.38	3.02	2.32	1.67	8.9
Eu	0.03	0.05	0.06	0.04	0.10	0.14	0.17	0.20	0.8
Gd	0.18	0.35	0.95	0.67	0.98	1.50	1.49	1.64	5.0
Tb	0.05	0.09	0.49	0.40	0.37	0.73	0.94	0.51	1.9
Dy	0.98	0.99	5.25	6.75	3.38	5.47	9.42	4.21	13.5
Ho	0.33	0.24	1.16	1.45	0.39	0.91	1.69	0.61	1.7
Er	1.91	1.32	5.63	7.29	1.19	2.53	6.09	2.69	6.3
Tm	0.88	0.52	2.68	3.19	0.60	0.98	2.25	0.89	2.2
Yb	16.73	9.96	44.94	53.97	11.63	13.49	33.12	17.35	34.1
Lu	1.78	1.28	5.48	5.99	1.27	1.19	2.86	1.80	3.8
$\sum$REE	25.30	16.59	96.97	94.45	84.84	105.75	194.80	382.11	390.90
δEu	0.55	0.60	0.20	0.28	0.27	0.20	0.28	0.37	0.36
δCe	2.01	1.69	1.88	1.74	1.89	2.05	1.88	1.59	1.91
t_3	0.21	0.19	0.70	0.90	1.04	0.92	1.09	0.65	0.95
t_4	1.20	0.17	0.20	0.18	0.40	0.33	0.25	0.27	0.25

33

$T_{3.4}$	0.59	0.30	0.47	0.52	0.60	0.56	0.58	0.48	0.55
U-Pb ages(Ma)	215.2	212.2	218.8	215.7	215.0	200.2	160.3	173.9	143.5

634   The third tetrad (t3), the fourth tetrad (t4), and the degree of the tetrad effect (TE3.4), were

635   calculated according to the method of Monecke et al. (2002).U-Pb ages were expressed by

636    $^{206}Pb/^{238}U$ ages.

637
638
639
640

34